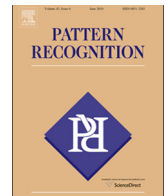




ELSEVIER

Contents lists available at ScienceDirect

Pattern Recognition

journal homepage: www.elsevier.com/locate/pr

Robust similarity registration technique for volumetric shapes represented by characteristic functions



Wanmu Liu^a, Sasan Mahmoodi^{a,*}, Tom Havelock^{b,c}, Michael J. Bennett^c

^a School of Electronics and Computer Science, University of Southampton, Southampton SO17 1BJ, United Kingdom

^b Faculty of Medicine, University of Southampton, Southampton SO16 6YD, United Kingdom

^c Southampton NIHR Respiratory Biomedical Research Unit, Southampton University Hospital NHS Foundation Trust, Southampton SO16 6YD, United Kingdom

ARTICLE INFO

Article history:

Received 23 January 2013

Received in revised form

10 August 2013

Accepted 13 August 2013

Available online 8 October 2013

Keywords:

Similarity registration

Volumetric shapes

Characteristic functions

Spherical cross-correlation

Phase correlation

Registration of lungs

ABSTRACT

This paper proposes a novel similarity registration technique for volumetric shapes implicitly represented by characteristic functions (CFs). Here, the calculation of rotation parameters is considered as a spherical cross-correlation problem and the solution is therefore found using the standard phase correlation technique facilitated by principal components analysis (PCA). Thus, fast Fourier transform (FFT) is employed to vastly improve efficiency and robustness. Geometric moments are then used for shape scale estimation which is independent from rotation and translation parameters. It is numerically demonstrated that our registration method is able to handle shapes with various topologies and robust to noise and initial poses. Further validation of our method is performed by registering a lung database.

© 2013 Elsevier Ltd. All rights reserved.

1. Introduction

1.1. Background

Shape registration is a fundamental technique in computer vision. It benefits a variety of research fields, such as statistical shape study, shape-based image segmentation, 3-D modeling of real world objects, which give rise to all kinds of registration techniques. Therefore, before a certain registration technique is developed, several aspects need to be taken into account:

Shape representations: The raw data acquired at hand may well differ in various research fields, and they are intended to be well suited for application purposes. For example, in real world object modeling, popular representations include range data [13,8,14] and point sets [5,3], while in shape-based image segmentation [25,26], parametric surfaces and signed distance functions (SDFs, [16]) are frequently used for curve/surface evolutions. In medical imaging, shapes are often represented by characteristic functions (CFs) which serve as mask to emphasize regions of interest.

Expected results of registration: In 3-D object modeling, a sequence of partial views represented by range data are to be registered for acquisition of a full 3-D object. This process involves

matching of common regions of surfaces. In shape-based image segmentation and statistical shape modeling, registration finds a suitable match of two entire shapes.

Degrees of precision: In fact, registration precision is closely associated with given degrees of freedom. Rigid transformation [3,8,2] involves rotation and translation and similarity registration further includes scale, while non-rigid transformation allows local deformation to achieve a greater matching. One can choose proper degrees of freedom according to the registration problem at hand. For example, entire shape or surface may be sufficiently matched by rigid transformation, however, more sophisticated modeling such as facial expression modeling or heart ventricle motion tracking involves non-rigid transformation [11].

Similarity/dissimilarity measure of registration: Most frequently used measure is a sum of squared distance/difference (SSD) between either explicit corresponding points or functions that used to represent shapes without explicit correspondence. Novel measures used in recent years include information theoretic measure between probability distribution functions estimated from point sets or signed distance functions [5,11,29] and kernel correlation of point sets entropy [28]. There are all kinds of measures to choose from, however, the measure should be well suited for the representations of shapes to achieve a satisfying result for registration.

The method proposed here is intended to be applied to two areas of research: statistical shape study of volumetric shapes and shape-based volumetric image segmentation. Considering the four aspects given above, the method could be described as follows.

* Corresponding author. Tel: +44 23 8059 3284; fax: +44 23 8059 4498.

E-mail addresses: w13g10@ecs.soton.ac.uk (W. Liu),

sm3@ecs.soton.ac.uk (S. Mahmoodi), t.havelock@soton.ac.uk (T. Havelock),

michael.bennett@soton.ac.uk (M.J. Bennett).

It concerns shapes represented by CFs. Anatomical structures acquired from medical images are mostly volumetric and characteristic functions that denote the regions of interest in a straightforward way. Also, in shape-based image segmentation, regions inside the reference shapes and the target areas of images are to be maximized, where CFs are a representation with simplicity.

It registers two entire shapes. In statistical modeling of volumetric shapes, one entire shape in volumetric image could be obtained through manual or computer-aided segmentation, which does not involve matching partial views (range data) together. The same goes with shape-based image segmentation, the target areas are intact shapes and they are to be registered with model shapes at hand.

It handles similarity registration that involves isometric scale, rotation and translation. Similarity registration is a precursor to statistical modeling of volumetric shapes. Furthermore, in the shape-based image segmentation, the first step to bring reference shape to segmentation process is similarity registration before any local deformation.

It uses region-based similarity measures between shapes. Region-based similarity measures between CFs denote the volume of homogeneous region of shapes. In statistical modeling of volumetric shapes, we focus more on the region features rather than the boundaries. With regard to the volumetric image segmentation, although it is ideal to achieve both region and boundary accuracy, the final results one would expect first are accurate regions. It should be pointed out that the registration is performed using all voxels inside shapes to be registered.

Let us now proceed to review several previous works that concern this topic.

1.2. Previous works

The method frequently used similarity registration is gradient descent optimization of shapes represented by SDFs. The shape-based segmentation method proposed in [6] involves rigid registration in 2-D using a variational framework. It handles registration by optimizing a proposed functional that iteratively registers the evolving contours to rigid shapes represented by level-set functions. Similar works are done in [27,4], who applied rigid/affine registration to statistical modeling of shapes and image segmentation process. Also, in [17], similarity registration is used as a pre-alignment technique for non-rigid registration. These works commonly choose SSD as the measure for similarity between shapes, which also suffer from local minima problem. Alternatively, it is proposed in [11] to maximize mutual information between SDFs of shapes and the method performs well in finding a global maximum.

The methods proposed in [1,15] have a close relationship with the works done in this paper. The calculations of rotation and translation parameters are related to standard correlation problems and scale parameter is computed using geometric metric moments of shapes. Experiments show that they have good robustness against occlusions, noise and topological differences. However, these methods are based on 2D and shapes are represented by SDFs, while the method proposed in this paper employs CFs as shape representation and designed for volumetric shapes.

Another method that concerns this topic is the iterative closed point (ICP) method introduced in [2] that solves general rigid registration problem (concerning rotation and translation). This method, at each iteration, finds the closest points on the surface of target shape to that of the reference shape and optimizes rotation and translation. Results indicate that it is suitable for a variety of representations of shapes including point sets, parametric surfaces and implicit surfaces represented by level-set functions. The ICP

method performs well in local optimization, however, when the poses of shapes to be registered have large differences, it may fall into local minima. Another disadvantage is that it is claimed to be slow. Accelerated ICP methods were later proposed in [21,9,23].

In recent years, the Laplace–Beltrami spectra employed as shape descriptors in [20,19,18,22] could be used to perform analyses of shapes regardless of their poses and scale. Our method has some similarities with these works. In the calculations of rotation and scale parameters, shapes are transformed into other representations. However, these works aim at evaluating similarity between shapes without registration for shape retrieval from database and quality assessment of data that represent surfaces and volumes.

The rest of the paper is organized as follows. Section 2 presents some mathematical preliminaries and statement of the problem concerning shape registration. Section 3 describes the theory behind the registration technique proposed here as well as some implementation remarks. Experimental results are presented in Section 4. Finally we conclude the paper and give future directions of the method in Section 5.

2. Mathematical preliminaries

2.1. Unit quaternions as representation of rotations

Unit quaternions are used as a mathematical representation of rotation of volumetric rigid shapes. A unit quaternion is a four vector $\vec{q} \in \mathbb{S}^3$, where $\mathbb{S}^3 = \{\mathbf{h} \in \mathbb{R}^4 : \|\mathbf{h}\| = 1\}$ ($\|\cdot\|$ is the Euclidean norm). \mathbb{S}^3 represents a unit sphere in 4-D Euclidean space, frequently referred to as unit 3-sphere. A volumetric rigid body could be considered as a set of 3-D vectors, and rotation of a vector set about a fixed axis is a linear transform and performed by a 3×3 matrix, denoted by \mathbf{R} with $\det(\mathbf{R}) = 1$. It is explained well in [7] that one unit quaternion \vec{q} generates one rotation matrix \mathbf{R} through the equation given in the footnote.¹ Next, we give a brief review of quaternion representation of rotation.

A unit quaternion in representation of rotation consists of a scalar part and a vector part, namely $\vec{q} = (\eta, \vec{v})$. It has a counterpart known as the ‘conjugate’, denoted by $\vec{q}^* = (\eta, -\vec{v})$. Multiplication of quaternions follows the formula below:

$$\vec{q}_1 \vec{q}_2 = (\eta_1 \eta_2 - \vec{v}_1 \cdot \vec{v}_2, \eta_1 \vec{v}_2 + \eta_2 \vec{v}_1 + \vec{v}_1 \times \vec{v}_2) \tag{1}$$

where ‘ \cdot ’ is the inner product of vectors and ‘ \times ’ their cross product. However, this multiplication is non-commutative. Multiplication of a set of unit quaternions in a particular order, namely $\vec{q} = \vec{q}_1 \vec{q}_2 \dots \vec{q}_N$, could produce one unique rotation and the corresponding inverse rotation could be produced by $\vec{q}^* = \vec{q}_N^* \dots \vec{q}_2^* \vec{q}_1^*$ (see Fig. 1 for an example).

More intuitively, a unit quaternion consists of an axis $\vec{a} \in \mathbb{S}^2$, where $\mathbb{S}^2 = \{\mathbf{x} \in \mathbb{R}^3 : \|\mathbf{x}\| = 1\}$, and an angle $\Delta\theta \in \mathbb{R}$, making $\vec{q}(\vec{a}, \Delta\theta) = (\cos(\Delta\theta/2), \vec{a}^T \sin(\Delta\theta/2))$. Vector \vec{a} and angle $\Delta\theta$ are considered as the axis and angle of rotation, following the right hand rule.

¹ Assuming that $\vec{q} = (q_0, q_1, q_2, q_3)$,

$$\mathbf{R}(\vec{q}) = \begin{pmatrix} q_0^2 + q_1^2 - q_2^2 - q_3^2 & 2(q_1 q_2 - q_0 q_3) & 2(q_1 q_3 + q_0 q_2) \\ 2(q_1 q_2 + q_0 q_3) & q_0^2 + q_2^2 - q_1^2 - q_3^2 & 2(q_2 q_3 - q_0 q_1) \\ 2(q_1 q_3 - q_0 q_2) & 2(q_2 q_3 + q_0 q_1) & q_0^2 + q_3^2 - q_1^2 - q_2^2 \end{pmatrix}$$

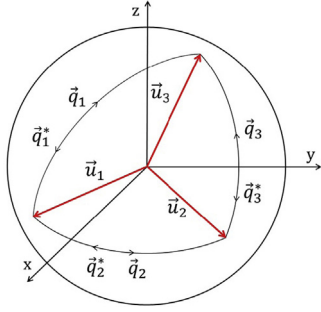


Fig. 1. \vec{u}_1 rotates to coincide \vec{u}_3 according to \vec{q}_1 , and the reverse rotation is generated by \vec{q}_1^* . An alternative path is $\vec{u}_1 \rightarrow \vec{u}_2 \rightarrow \vec{u}_3$, produced by $\vec{q}_2 \vec{q}_3$ and the path back is according to $\vec{q}_3^* \vec{q}_2^*$.

2.2. Implicit representation of volumetric shapes

Let $\Omega \subset \mathbb{R}^3$ be bounded and represent the image domain, and $\mathcal{X}_r(\mathbf{x}) : \Omega \rightarrow \mathbb{R}$ and $\mathcal{X}_t(\mathbf{x}) : \Omega \rightarrow \mathbb{R}$ denote the characteristic functions (CFs) of reference shapes and target shapes. These functions are defined as

$$\mathcal{X}(\mathbf{x}) = \begin{cases} 1, & \mathbf{x} \in \Omega_+, \\ 0, & \mathbf{x} \in \Omega_-, \end{cases} \quad (2)$$

where Ω_+ and Ω_- respectively represent domains inside and outside shapes. The surfaces of shapes are implicit and of less importance in this work.

This is a convenient representation especially in medical imaging, which mostly requires masks that emphasize region of interest (ROI). Furthermore, it is non-parametric and naturally handle shape topologies, which could be associated with signed distance functions (SDFs) that facilitate deformation and statistical study of shapes. In later experiments, we show that it is, furthermore, a statistically robust representation that is insensitive to outliers.

3. Method

3.1. An initial transformation

It is frequently assumed that in the similarity registration of two shapes, the reference shape is scaled, rotated and translated to match the target shape. To facilitate calculations of registration parameters, principal component analysis (PCA) is used here to do a coarse match of shapes.

Let $\mathbf{c} \in \mathbb{R}^3$ denote the centroid of \mathcal{X} in the initial Cartesian coordinate system. \mathbf{c} is calculated by

$$\mathbf{c} = \frac{\int_{\Omega} \mathbf{x} \mathcal{X}(\mathbf{x}) d\mathbf{x}}{\int_{\Omega} \mathcal{X}(\mathbf{x}) d\mathbf{x}} \quad (3)$$

Then 3×3 symmetric covariance matrix Σ could therefore be obtained from

$$\Sigma = \frac{\int_{\Omega} (\mathbf{x} - \mathbf{c})(\mathbf{x} - \mathbf{c})^T \mathcal{X}(\mathbf{x}) d\mathbf{x}}{\int_{\Omega} \mathcal{X}(\mathbf{x}) d\mathbf{x}} \quad (4)$$

Σ_r and Σ_t respectively for reference and target shapes could be computed using the above equation. We then calculate the respective three eigenvectors of Σ_r and Σ_t , denoted by $\mathbf{P}_r = (\vec{p}_{r_1}, \vec{p}_{r_2}, \vec{p}_{r_3})$ and $\mathbf{P}_t = (\vec{p}_{t_1}, \vec{p}_{t_2}, \vec{p}_{t_3})$. The eigenvectors are ordered according to their eigenvalues, i.e. the first eigenvector corresponds to the largest eigenvalue (see Fig. 2). These three eigenvectors are referred to in this paper as the first, second and third principal axes. $\mathcal{X}_r(\mathbf{x})$ is then translated and rotated so that \mathbf{P}_r

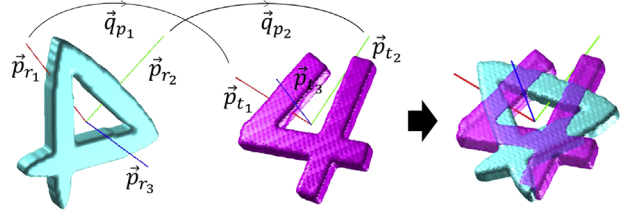


Fig. 2. The process of coinciding principal axes of shapes to be registered. The first, second and third principal axes of shapes are marked by vectors.

is coincided with \mathbf{P}_t , and \mathbf{P}_t is used as the axes of the new Cartesian coordinates. This rotation is generated by \vec{q}_p , which is calculated by three steps:

Step 1: Calculating \vec{q}_{p_1} that coincides the first principal axis,

$$\begin{aligned} \Delta\theta_{p_1} &= \cos^{-1}(\vec{p}_{r_1} \cdot \vec{p}_{t_1}), \\ \vec{a}_{p_1} &= (\vec{p}_{r_1} \times \vec{p}_{t_1}) / \sin(\Delta\theta_{p_1}), \\ \vec{q}_{p_1} &= (\cos(\Delta\theta_{p_1}/2), \vec{a}_{p_1} \sin(\Delta\theta_{p_1}/2)), \end{aligned}$$

Step 2: Calculating \vec{q}_{p_2} that coincides the second principal axis,

$$\begin{aligned} \Delta\theta_{p_2} &= \cos^{-1}(\mathbf{R}(\vec{q}_{p_1})\vec{p}_{r_2} \cdot \vec{p}_{t_2}), \\ \vec{a}_{p_2} &= (\mathbf{R}(\vec{q}_{p_1})\vec{p}_{r_2} \times \vec{p}_{t_2}) / \sin(\Delta\theta_{p_2}), \\ \vec{q}_{p_2} &= (\cos(\Delta\theta_{p_2}/2), \vec{a}_{p_2}^T \sin(\Delta\theta_{p_2}/2)), \end{aligned}$$

Step 3: Calculating \vec{q}_p by quaternion multiplication of \vec{q}_{p_1} and \vec{q}_{p_2} ,

$$\vec{q}_p = \vec{q}_{p_1} \vec{q}_{p_2},$$

In certain cases the third principal axes may be inverse to each other after the coinciding, however, this would not affect the final result, because the third principal axes are statistically of less significance. $\mathcal{X}_r(\mathbf{x})$ and $\mathcal{X}_t(\mathbf{x})$ are thus brought into the new coordinate system i.e.:

$$\tilde{\mathcal{X}}_r(\mathbf{x}) = \mathcal{X}_r(\mathbf{R}(\vec{q}_p)(\mathbf{x} + \mathbf{c}_r)), \quad (5)$$

$$\tilde{\mathcal{X}}_t(\mathbf{x}) = \mathcal{X}_t(\mathbf{x} + \mathbf{c}_t), \quad (6)$$

where \mathbf{c}_r and \mathbf{c}_t are the respective centroids of CFs. Fig. 2 presents a general process of coinciding shapes' principal axes.

3.2. Scaling

Geometric moments of CFs are employed here to calculate scale difference of shapes. Let $s \in (0, +\infty)$ denote the scale parameter. We start with considering a simple case that the target shape is the scaled version of the reference shape, therefore, their CFs are related to each other with respect to s by the following equation:

$$\tilde{\mathcal{X}}_t(\mathbf{x}) = \tilde{\mathcal{X}}_r(s\mathbf{x}) \quad (7)$$

The geometric moments of $\tilde{\mathcal{X}}_r(\mathbf{x})$ and $\tilde{\mathcal{X}}_t(\mathbf{x})$ are given as

$$G_r(m) = \int_{\Omega} \|\mathbf{x}\|^m \tilde{\mathcal{X}}_r(\mathbf{x}) d\mathbf{x}, \quad (8)$$

$$G_t(m) = \int_{\Omega} \|\mathbf{x}\|^m \tilde{\mathcal{X}}_t(\mathbf{x}) d\mathbf{x}, \quad (9)$$

where $m = 0, 1, 2, \dots, M$ is the degree of the moments and $\|\cdot\|$ is the Euclidean norm. Substituting Eqs. (7)–(9), assuming $\mathbf{x} = s\mathbf{x}$, we have

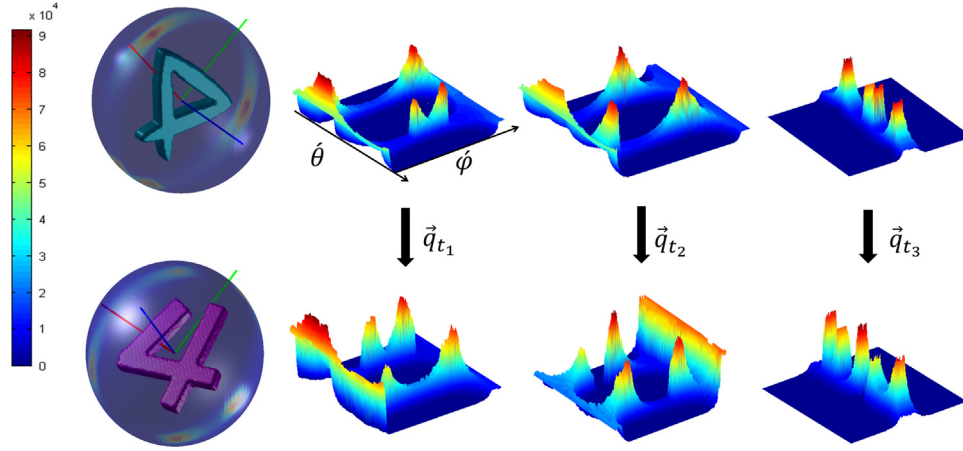


Fig. 3. An example of the rotation adjustments. The top row from left to right is the S^2 map, $\mathcal{R}_{\vec{a}}^2$ maps obtained according to \vec{p}_{r_1} , \vec{p}_{r_2} , \vec{p}_{r_3} of the reference ‘4’. The bottom row from left to right is S^2 map and $\mathcal{R}_{\vec{a}}^2$ maps of the target ‘4’ ordered in the same way. From each $\mathcal{R}_{\vec{a}}^2$ map one quaternion for rotation adjustment is calculated and there are in total three quaternions, namely \vec{q}_{t_1} , \vec{q}_{t_2} , and \vec{q}_{t_3} .

$$G_t(m) = \int_{\Omega} \|\mathbf{x}\|^m \tilde{\chi}_r(s\mathbf{x}) d\mathbf{x} = \int_{\Omega} \frac{\|\tilde{\mathbf{x}}\|^m}{s^m} \tilde{\chi}_r(\tilde{\mathbf{x}}) \frac{d\tilde{\mathbf{x}}}{s^3} = \frac{1}{s^{m+3}} \int_{\Omega} \|\tilde{\mathbf{x}}\|^m \tilde{\chi}_r(\tilde{\mathbf{x}}) d\tilde{\mathbf{x}} = \frac{1}{s^{m+3}} G_r(m) \quad (10)$$

The logarithms of both sides hold the equality

$$\ln G_t(m) = \ln \frac{1}{s^{m+3}} G_r(m) \quad (11)$$

However, shapes to be registered have differences in practice, therefore we minimize the squared difference of both sides. Let E_M be the sum of the scale error with degree m given by

$$E_M = \sum_{m=0}^M \left| \ln G_t(m) - \ln \frac{1}{s^{m+3}} G_r(m) \right|^2 = \sum_{m=0}^M \left| (m+3) \ln s + \ln \frac{G_t(m)}{G_r(m)} \right|^2 \quad (12)$$

Finally, the optimal scale parameter s_{op} is estimated by minimizing E_M :

$$s_{op} = \underset{s}{\operatorname{argmin}} E_M \quad (13)$$

3.3. Rotation

An optimal rotation could be represented by a unit quaternion \vec{q}_{op} which consists of a unit vector \vec{a}_{op} and an angle $\Delta\theta_{op}$ (explained in Section 2.1). To find \vec{a}_{op} and $\Delta\theta_{op}$, $\tilde{\chi}_r(\mathbf{x})$ and $\tilde{\chi}_t(\mathbf{x})$ are mapped to a spherical coordinate system for convenience. Let $\Omega_{S^2} \subset \mathbb{R} \times \mathbb{S}^2$ denote a spherical domain inside image domain Ω , and Ω_{S^2} is bounded with radius R . Then $\tilde{\chi}_r(\mathbf{x})$ and $\tilde{\chi}_t(\mathbf{x})$ are respectively represented by $\tilde{\chi}_r(\mathbf{r}) : \Omega_{S^2} \rightarrow \mathbb{R}$ and $\tilde{\chi}_t(\mathbf{r}) : \Omega_{S^2} \rightarrow \mathbb{R}$, where $\mathbf{r} = (r, \hat{\mathbf{x}}(\theta, \varphi))^T$ ($\hat{\mathbf{x}} = (\cos(\theta) \sin(\varphi), \sin(\theta) \sin(\varphi), \cos(\varphi))^T$). Moreover, $r \in [0, R]$, $\theta \in [0, 2\pi)$, and $\varphi \in [0, \pi]$.

Radial variable r contains scale difference between the shapes to be registered, therefore to remove its impact on calculating rotation angle of the two CFs, we integrate the CFs over variable r , i.e.:

$$\tilde{\chi}_r(\hat{\mathbf{x}}(\theta, \varphi)) = \int_0^R \tilde{\chi}_r(\mathbf{r}) r^2 dr, \quad (14)$$

$$\tilde{\chi}_t(\hat{\mathbf{x}}(\theta, \varphi)) = \int_0^R \tilde{\chi}_t(\mathbf{r}) r^2 dr. \quad (15)$$

This indeed could be intuitively considered as projecting the CFs of shapes onto a parametric unit sphere centered by their

centroids, referred to in this paper as S^2 maps (see Fig. 3). It should be noted that S^2 maps are not Gaussian maps which are generated according to the surface of shapes, while \mathcal{S}^2 maps are calculated using volumes of shapes. The problem is generalized to maximize the inner product of the two S^2 maps:

$$\begin{aligned} \vec{q}_{op} &= \underset{\vec{q}}{\operatorname{argmax}} \int_{S^2} \tilde{\chi}_t(\hat{\mathbf{x}}) \tilde{\chi}_r(\mathbf{R}(\vec{q})\hat{\mathbf{x}}) d\hat{\mathbf{x}} \\ &= \underset{\vec{q}}{\operatorname{argmax}} \langle \tilde{\chi}_t(\hat{\mathbf{x}}), \tilde{\chi}_r(\mathbf{R}(\vec{q})\hat{\mathbf{x}}) \rangle \end{aligned} \quad (16)$$

\vec{q}_{op} calculated from this term is not affected by the scale of shapes according to the following lemma.

Lemma. The optimal rotation parameter \vec{q}_{op} calculated using Eq. (16) is scale invariant.

The proof of this lemma is presented in the appendix.

In fact, Eq. (16) is a spherical cross correlation problem described in [10,12] as finding $\vec{q}_{op} \in SO(3)^2$ that maximizes $\langle \tilde{\chi}_t(\hat{\mathbf{x}}), \tilde{\chi}_r(\mathbf{R}(\vec{q})\hat{\mathbf{x}}) \rangle$. The solution to this problem is given in these works using fast Fourier transform (FFT) in $SO(3)$. However, the solution proposed in this paper is based on phase correlation.

The unit sphere is mapped onto a bounded plane with coordinates $\hat{\theta}$ and $\hat{\varphi}$, referred to in this paper as an $\mathcal{R}_{\vec{a}}^2$ map. The reason for using ‘ \vec{a} ’ as a subscript is that an $\mathcal{R}_{\vec{a}}^2$ map is generated according to a chosen rotation axis \vec{a} . Different choices of rotation axis \vec{a} generate different $\mathcal{R}_{\vec{a}}^2$ maps. In our case, three maps are generated according to the three principal axes \vec{p}_{t_1} , \vec{p}_{t_2} and \vec{p}_{t_3} (see Fig. 3).

Thus, $\tilde{\chi}_r(\mathbf{R}(\vec{q}(\vec{a}, \Delta\theta))\hat{\mathbf{x}}(\theta, \varphi)) \cong \tilde{\chi}_r(\hat{\theta} - \Delta\theta, \hat{\varphi})$, namely, the rotations of an S^2 map around an axis \vec{a} could be represented by simple shifts of the corresponding $\mathcal{R}_{\vec{a}}^2$ map along its $\hat{\theta}$ -axis. Assume that the 1-D Fourier transform of $\tilde{\chi}_r(\hat{\theta}, \hat{\varphi})$ and $\tilde{\chi}_t(\hat{\theta}, \hat{\varphi})$ with respect to $\hat{\theta}$ is respectively $\hat{\mathcal{Y}}_r(\omega_{\hat{\theta}}, \hat{\varphi})$ and $\hat{\mathcal{Y}}_t(\omega_{\hat{\theta}}, \hat{\varphi})$. The optimal rotation angle by rotating around a fixed common axis \vec{a}_0

² $SO(3) = \{\vec{q} \in \mathbb{R}^4 : \|\vec{q}\| = 1\}$ is a group of unit quaternions.

could be obtained by

$$\Delta\theta_{op}(\vec{a}_0) = \operatorname{argmax}_{\Delta\theta} \int_0^\pi \int_{-\infty}^{+\infty} \hat{y}_t(\omega_\theta, \hat{\phi}) \overline{\hat{y}_r(\omega_\theta, \hat{\phi})} e^{i\omega_\theta \Delta\theta} \sin(\hat{\phi}) d\omega_\theta d\hat{\phi} \quad (17)$$

Thus, fine rotational angles are adjusted sequentially around all three principal axes using Eq. (17). The order of adjustments is from the first principal axis to the third (see Fig. 4). Finally \vec{q}_{op} could be obtained by

$$\vec{q}_{op} = \vec{q}_p \vec{q}_{t_1} \vec{q}_{t_2} \vec{q}_{t_3}, \quad (18)$$

where \vec{q}_p is the quaternion that coincides principal axes of shapes (see Section 3.1) and \vec{q}_{t_1} , \vec{q}_{t_2} , \vec{q}_{t_3} are respectively the quaternions calculated using Eq. (17) for the three principal axes \vec{p}_{t_1} , \vec{p}_{t_2} and \vec{p}_{t_3} .

It should be pointed out that in implementation, one \mathcal{R}_d^2 map is directly calculated from CFs of shapes, and the other two maps are then computed from the first map. One can simply transform CFs of shapes into a spherical coordinate system with axes ‘ $r-\hat{\theta}-\hat{\phi}$ ’ and calculate sum of all voxels along the r -axis. The coordinate of each point on an \mathcal{R}_d^2 map can be represented by a unit three vector and these vectors could be used to calculate where the value of the current point should be assigned when ‘rotating’ the \mathcal{R}_d^2 map. The notion of S^2 map serves only as an intuition to explain the theory, however, it is not used in implementation.

The accuracy of rotation adjustments is determined by the number of sample points (resolution) of an \mathcal{R}_d^2 map. Bandwidth B

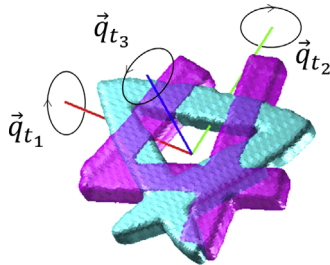


Fig. 4. The process of fine rotational adjustments. It is sequentially done in a ‘ $\vec{p}_{t_1} \rightarrow \vec{p}_{t_2} \rightarrow \vec{p}_{t_3}$ ’ manner.

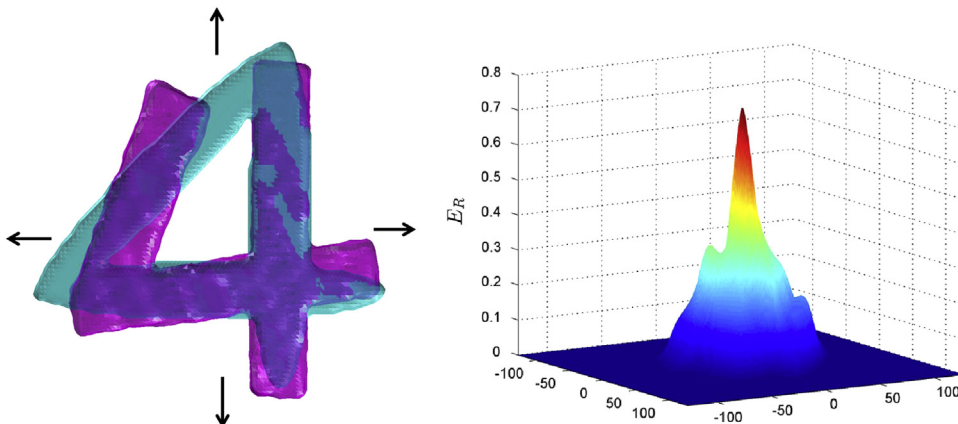


Fig. 5. Left: the open ‘4’ is fixed while the closed ‘4’ translates in two directions from –128 to 128. Right: the normalized inner products of shapes E_R (defined in Section 3.5) under different values of translation.

is used here to denote the sample density and π/B and $\pi/2B$ respectively represent the sample intervals of $\hat{\theta}$ and $\hat{\phi}$. Therefore, there are in total $4B^2$ points on an \mathcal{R}_d^2 map. This convention could be found in [12]. More discussions about bandwidth B are presented in Section 4.

3.4. Translation

Using the calculated scale and rotation parameters, s_{op} and \vec{q}_{op} , we obtain $\hat{x}_r(\mathbf{x}) = \mathcal{X}_r(s_{op} \mathbf{R}(\vec{q}_{op}) \mathbf{x})$. The problem is now to maximize the inner product of the CFs that represent the two shapes:

$$\begin{aligned} \vec{T}_{op} &= \operatorname{argmax}_{\vec{T}} \int_{\Omega} \mathcal{X}_t(\mathbf{x}) \hat{x}_r(\mathbf{x} - \vec{T}) d\mathbf{x} \\ &= \operatorname{argmax}_{\vec{T}} \langle \mathcal{X}_t(\mathbf{x}), \hat{x}_r(\mathbf{x} - \vec{T}) \rangle \end{aligned} \quad (19)$$

where $\vec{T} \in \mathbb{R}^3$ denotes the translation parameter. Assuming that $\hat{y}_r(\omega)$ and $\mathcal{Y}_t(\omega)$ are respectively the 3-D spatial Fourier transform of $\hat{x}_r(\mathbf{x})$ and $\mathcal{X}_t(\mathbf{x})$, the optimal translation parameter \vec{T}_{op} could be computed using

$$\vec{T}_{op} = \operatorname{argmax}_{\vec{T}} \int_{\mathbb{R}^3} \mathcal{Y}_t(\omega) \overline{\hat{y}_r(\omega)} e^{i\omega \cdot \vec{T}} d\omega, \quad (20)$$

where $\omega \in \mathbb{R}^3$ is the spatial frequency vector. The normalized inner products of shapes to be registered under different values of translation parameters are demonstrated in Fig. 5. Two typical directions of translation in $[-128, 128]$ are selected and two local maximum adjacent to the global peak could be observed in Fig. 5, right. It is important to note that the method proposed here is not affected by these local maxima. Further experiments addressing this issue could be found in Section 4. Although the calculations of rotation and scale are independent, translation optimization relies on how well the rotation and scale are estimated, namely \vec{T}_{op} varies with s_{op} and \vec{q}_{op} .

3.5. Similarity measures for evaluation of registration

After the shapes are registered using the method proposed here, some similarity/dissimilarity measures are supposed to be chosen for the evaluation of registration results. Several measures regarding region similarity in [24] are adopted here to achieve this

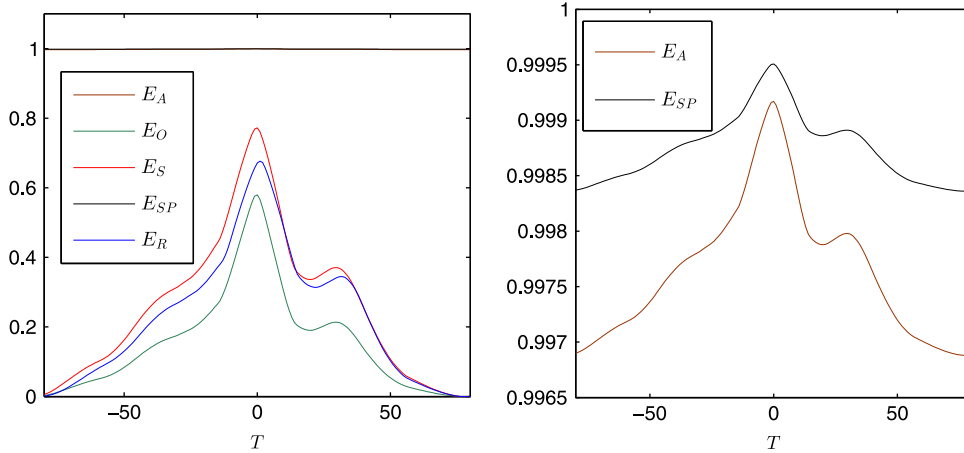


Fig. 6. The plots of similarity measures while the reference ‘4’ (similar to Fig. 5) translates from –80 to 80 along one direction. Left: accuracy, overlap, sensitivity, specificity and the normalized inner product. Right: only accuracy and specificity (their appearances are similar to the other three, however, they are impractical to be used in combination with the other three.)

task. Namely, normalized inner product, accuracy, overlap, sensitivity and specificity.

1. The normalized inner product of CFs of shapes denoted by E_R :

$$E_R = \int_{\Omega} \frac{\mathcal{X}_t(\mathbf{x})\mathcal{X}_r(s_{op}\mathbf{R}(\vec{q}_{op})\mathbf{x} - \vec{T}_{op})}{\|\mathcal{X}_t(\mathbf{x})\|_2 \|\mathcal{X}_r(s_{op}\mathbf{R}(\vec{q}_{op})\mathbf{x} - \vec{T}_{op})\|_2} d\mathbf{x} \quad (21)$$

where $\|\cdot\|_2$ is the L^2 -norm of CFs.³

The normalized inner product between shapes represented by CFs measures the volume of homogeneous region inside shapes. This measure is equivalent to the similarity angle presented in [24] and is suitable to measure similarity not only between two shapes, but also among a group of shapes. One of the issues in statistical shape modeling is to decide which sample shape is to be used as a standard. Normalized inner product is used to compare the registration results when different shapes are chosen as the standard (examples are given in Section 4.4.2).

2. Let us denote accuracy, overlap, sensitivity and specificity, respectively by E_A, E_O, E_S, E_{SP} :

$$E_A = \frac{V_1 + V_2}{V} \quad (22)$$

$$E_O = \frac{V_1}{V_1 + V_3 + V_4} \quad (23)$$

$$E_S = \frac{V_1}{V_1 + V_3} \quad (24)$$

$$E_{SP} = \frac{V_2}{V_2 + V_4} \quad (25)$$

where V stands for the volume of the image domain, V_1 the volume of common region of both shapes, V_2 the volume outside both regions of shapes, V_3 the volume of region inside \mathcal{X}_t but outside \mathcal{X}_r , and V_4 the volume of the region inside \mathcal{X}_r but outside \mathcal{X}_t . Two of the four measures, namely E_O and E_S , would be used in the experiments due to the fact that E_A and E_{SP} are too close to 1 (between 0.995 and 1). A primary comparison of the similarity measures can be found in Fig. 6.

In shape-based image segmentation, especially ROI extraction, region accuracy is of greater significance than boundary accuracy. Therefore, similarity registration used in the segmentation process should maximize the homogeneous region between the reference

shape and internal area of evolving surfaces. In previous methods, such as ICP, the sum of squared difference or distance (SSD) between explicit corresponding points on shapes’ surfaces is used as the measure, which is dependent on the accuracy of locating corresponding points and can be largely affected by noise and initial poses.

4. Experimental results

In this section, a series of experiments is presented here to show the performance of the proposed technique. Initially, synthetic shapes with various topologies are registered as a primary test stage to show the method proposed here is able to deal with relatively difficult shapes. A comparison is then presented between our method and the classical ICP method to show that our method barely suffers from traditional local minima problem. Next, several performance analyses are given here to show accuracy, efficiency, stability and robustness of our method. In addition, the performance analyses mainly concern scale and rotation parameters, which are the major part of the method proposed here. Lastly, we give two examples for the applications of the method: registration in shape-based image segmentation and in statistical modeling of shapes. Shapes of lungs involved in this stage are mask images.

The method proposed here is implemented in MATLAB 2012b on a PC station with a 2.67 GHz Xeon processor and 12 GB RAM. Reference shapes are in cyan (light color), target shapes in magenta (deep color) and for visualization purposes, only the surface of the shapes are shown here.

4.1. Registration of topologically different shapes

Some primary experiments are presented here to show the method proposed here works with shapes with complex topologies. Fig. 7 demonstrates the registration of topologically different ‘4’s extended from the 2-D image. By the feature points corresponding method, the number of feature points involved may well be different, due to their difference in Euler characteristic numbers. Such a difference in the number of feature points makes the additional handling of the topology more difficult, while such a difference has no impact on the technique proposed here.

A more complex case of registering two shapes with various topologies is presented in Fig. 8. The reference shape is two linked symmetric rings whereas the target shape consists of two

³ $\|\mathcal{X}\|_2 = (\int_{\Omega} |\mathcal{X}|^2 d\mathbf{x})^{1/2}$.

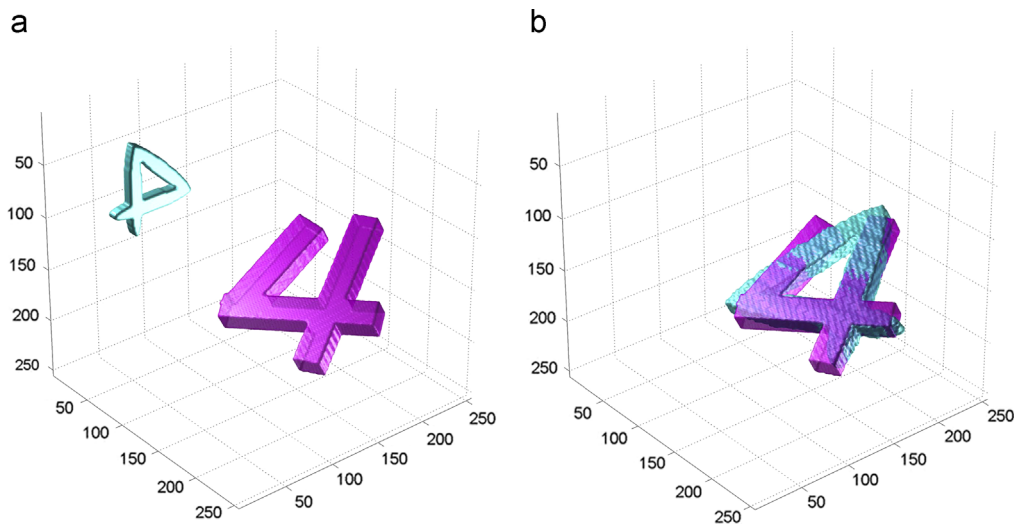


Fig. 7. The registration of topologically different '4's. (a) The reference shape (a closed '4') and the target shape (an open '4'). (b) The result obtained by the technique proposed here. (For interpretation of the references to color in this figure caption, the reader is referred to the web version of this article.)

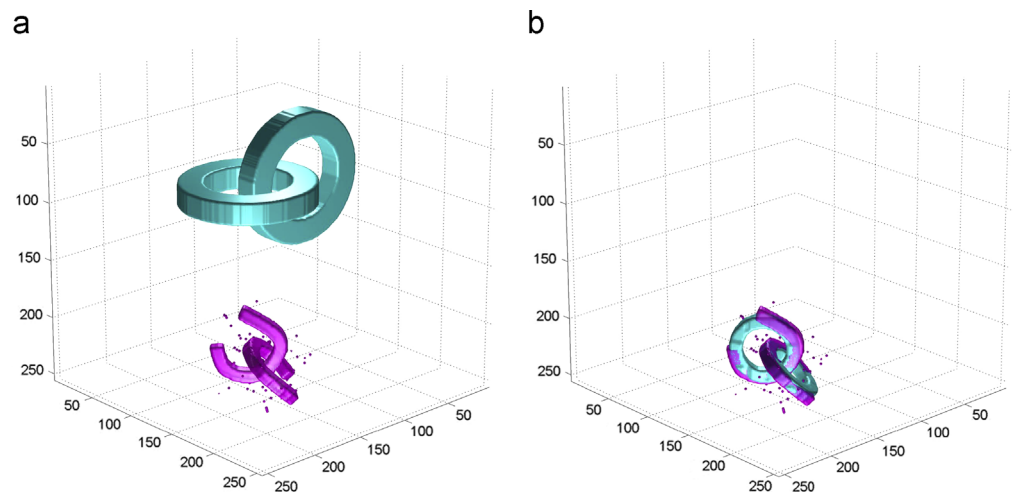


Fig. 8. The registration of a regular and an irregular shape with different topologies. (a) The reference shape (two linked rings) and the target shape (two linked horseshoes). (b) The result of registration.

unsymmetric horseshoes with some manually added clutters. However, such a topological variation and the clutters have no impact on the technique proposed here.

Some data concerning registration are provided in Table 1, including Image size, approximate scopes of shapes, maximum degree of moments M , bandwidth B (this parameter is explained in the last paragraph of Section 3.3), the execution time t of our algorithm and registration parameters.

4.2. A comparison with the state-of-art methods

The classical ICP method is implemented here to compare with the technique proposed here. The ICP method is able to handle the registration of shapes in a variety of representations and in the case of CFs, only the boundary voxels are considered in the calculations. Also, shapes represented by CFs could be viewed as a particular type of image (mask image), therefore the similarity image registration algorithm available in MATLAB is used here to do the comparison. The size of the target '4' is reduced here for comparison of the purposes and the reference '4' is rescaled using calculated s_{op} . One major purpose of this comparison is to address the local minima issue that affects most registration methods.

Table 1

Some data concerning registrations performed in this section.

Registration data	'4's	Linked rings and horseshoes
Image size	$256 \times 256 \times 256$	$256 \times 256 \times 256$
Reference shape size	$80 \times 80 \times 10$	$120 \times 120 \times 170$
Target shape size	$150 \times 150 \times 20$	$60 \times 60 \times 90$
M	5	5
B	128	128
t (s)	3.55	5.43
s_{op}	1.85	0.47
\vec{q}_{op}	(-0.66, 0.38, -0.65, -0.03)	(0.52, 0.70, -0.02, 0.50)
\vec{T}_{op}	(89, 102, -93) ^T	(104, 96, -96) ^T

Three typical initial poses of the reference '4' shown on the top row of Fig. 9 are used here to register the two shapes.

The left column of Fig. 9 demonstrates that the ICP method falls into a local minimum using the first initial pose. The second initial pose is the result of coinciding the principal axes, which is suggested in [2]. However, the ICP method falls into the same local minimum. Finally, we manually adjust the pose of the

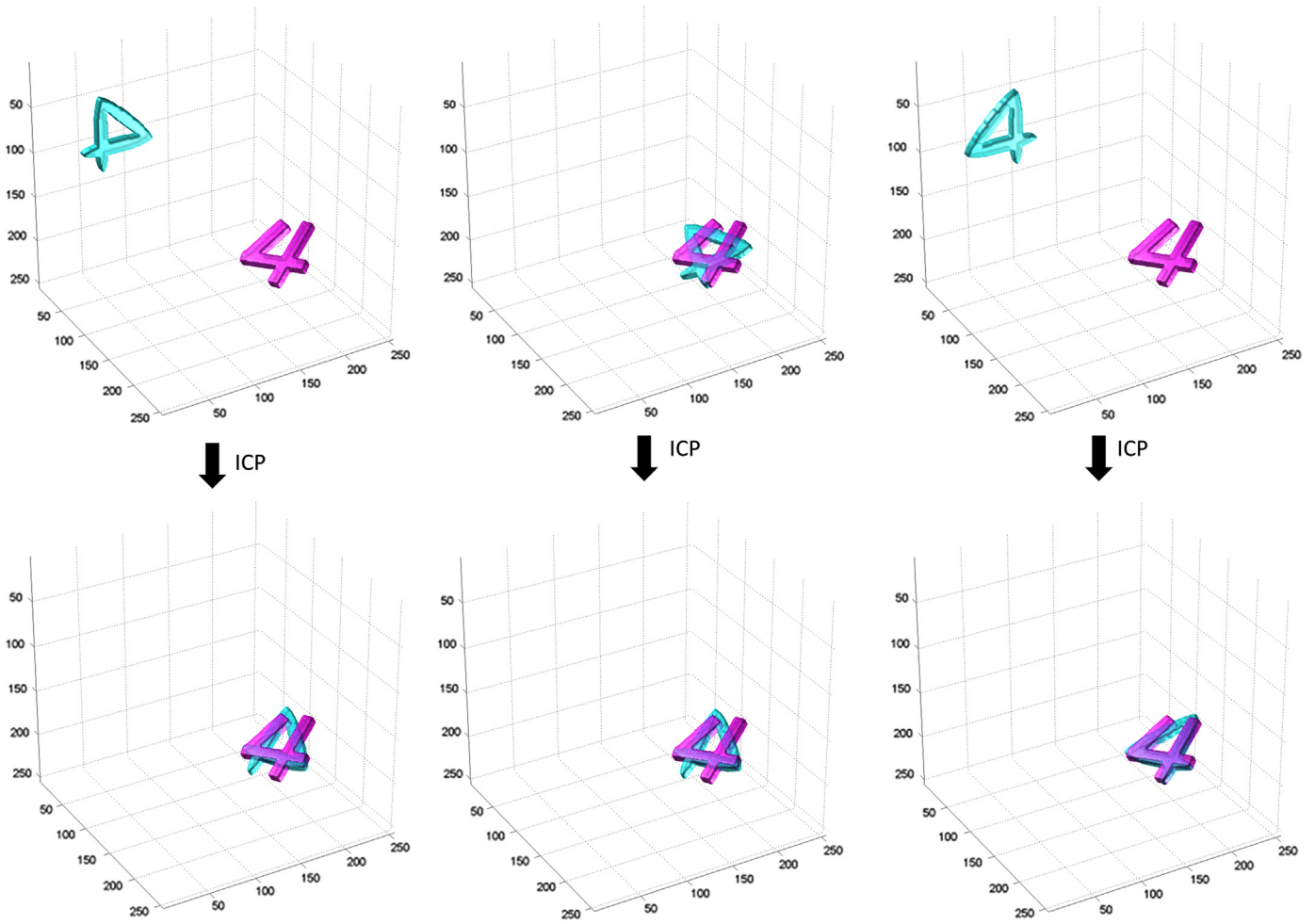


Fig. 9. From left to right on the top row are three initial poses chosen here to do the comparison. The corresponding registration results using the ICP method are shown on the bottom row. Particularly, the initial pose shown in the middle on the top row is the result of coinciding the principal axes of shapes.

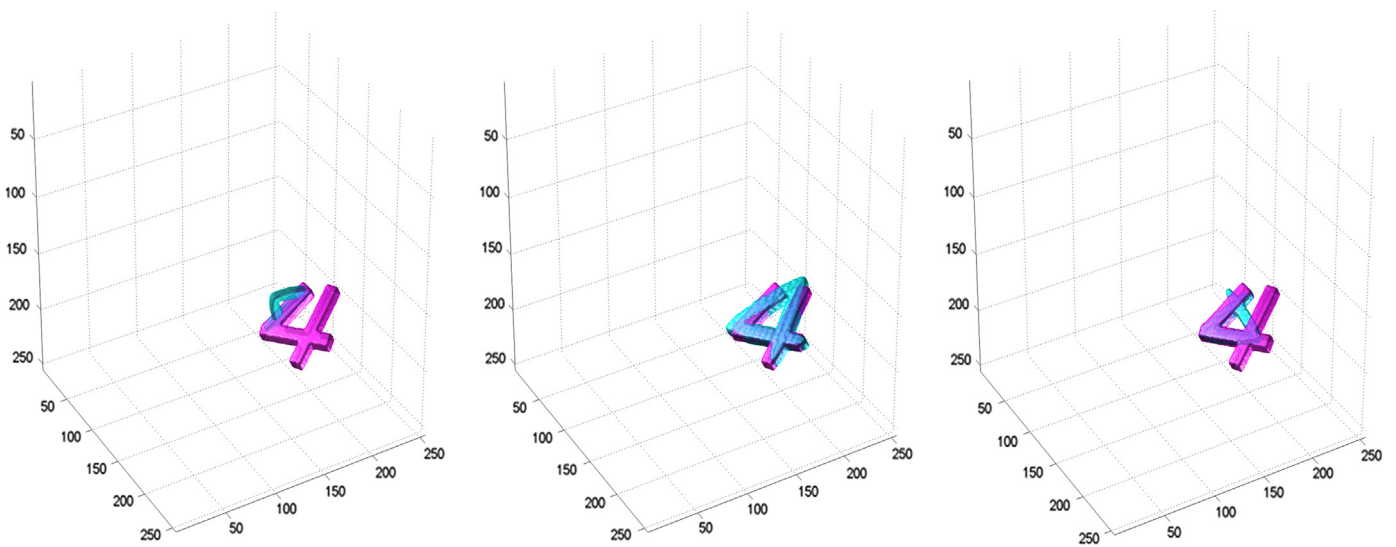


Fig. 10. From left to right are the results of the MATLAB registration method under the three initial conditions showed in Fig. 9.

reference '4', which is shown on the right column of Fig. 9, and the ICP method gives a satisfying result. This also indicates that the ICP method does well in registering shapes of various topologies with appropriate initial poses.

With regard to execution time, the ICP method takes 16.01 s (50 iterations) from the pose on the top left in Fig. 9, 11.79 s (31 iterations) for the top middle in Fig. 9 and 11.31 s (29 iterations) for the top right in Fig. 9. In fact, the volumetric implementation of

the ICP method is generally efficient, because there is no need for calculation of the corresponding closest points during each iteration once the preprocessing (calculating Euclidean distance map, which takes on average 4.8 s) is done. Average 0.225 s for each iteration is mostly spent on extracting boundary voxels and rotation. In contrast, our algorithm takes 1.33 s ($B=128$) to calculate rotation parameter given arbitrary initial pose.

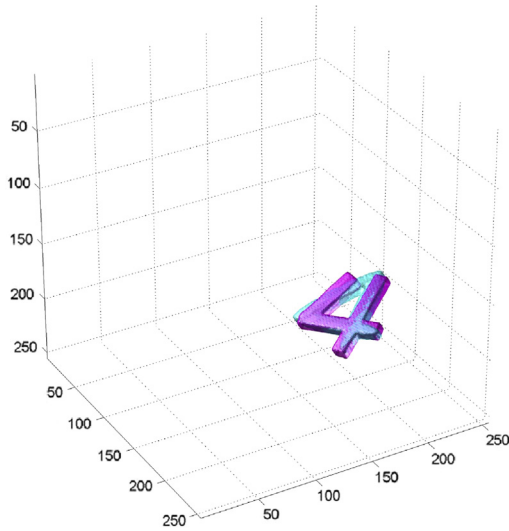


Fig. 11. The registration result of our method using the three initial poses in Fig. 9.

Fig. 10 presents the results of registration using the MATLAB registration algorithm corresponding to the three initial poses in Fig. 9. Fig. 10, left and right, indicates that the method falls into local minima while Fig. 10, middle, gives a correct result of the registration. However, the execution time needed from left to right is respectively 83.11 s, 109.81 s and 103.90 s. Admittedly, the image registration method is not specifically designed for shape registration and fails under certain conditions.

The registration results for all three initial poses using our method are shown in Fig. 11. Only one picture is given here because the results achieved by our method are the same for all three initial poses. In addition, the ICP method handles translation by simply coinciding the centroids of shapes to be registered, which may not be optimal.

In addition, the intermediate result after coinciding the principal axes given on the top middle image in Fig. 9 suggests that PCA provides only a coarse match of the two shapes and further fine adjustments are necessary.

4.3. Performance analyses

Two aspects of the technique are given to analyze its performance: one is accuracy and efficiency, and the other is stability. The reference shape and the target shape chosen for the analyses in this section are the same in Section 4.2, namely, two volumetric '4's. The major parts of the method proposed here are the calculations of scale and rotation parameters, therefore, extensive analyses are performed for these two parameters.

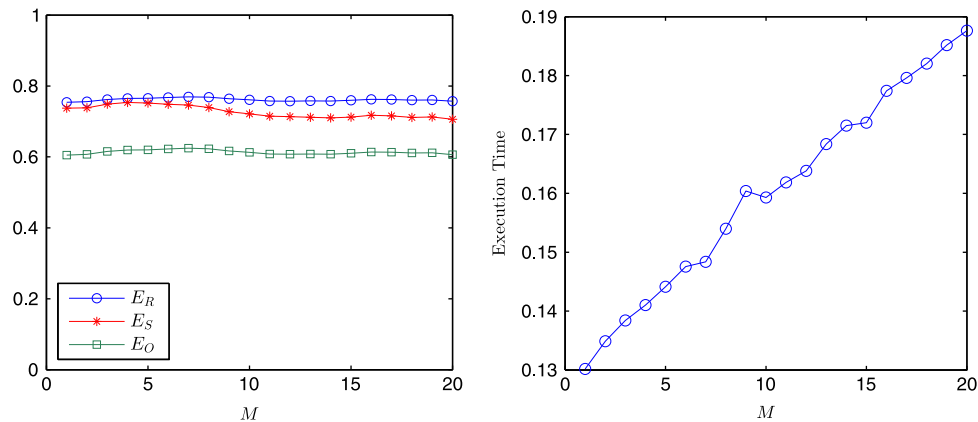


Fig. 12. Normalized inner product between shapes (left) and time needed for estimating s_{op} (right) using different values of M .

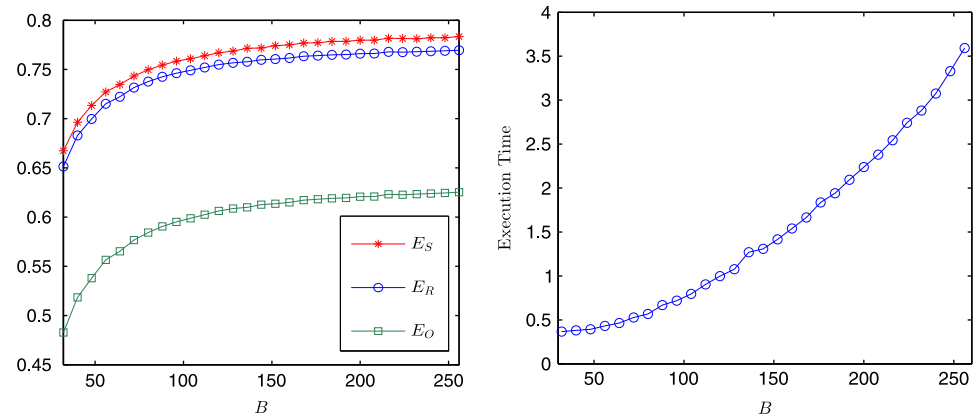


Fig. 13. Normalized inner product between shapes after registration (left) and execution time using different bandwidth B (right).

4.3.1. Accuracy vs. efficiency

Different values of M and B are chosen to demonstrate their impacts upon accuracy and efficiency of the proposed technique.

Fig. 12 presents the relationship among similarity measures, execution time and M . In the computation of the similarity measures, a fixed large bandwidth ($B=256$) is used and the corresponding \vec{T}_{op} is recalculated when M is changed. As observed from Fig. 12, the increase of M does not significantly change the value of those similarity measures and only prolongs the time needed for scale estimation. Therefore, lower degrees of geometric moments are sufficient to estimate s .

Fig. 13 demonstrates the relationship among the similarity measures, execution time and bandwidth B . Trade-off between accuracy and efficiency with respect to bandwidth could be observed from the plot on the left in Fig. 13. The inner product increases as bandwidth becomes larger, while more time is needed for numerical computations. Again, M is fixed and \vec{T}_{op} is recalculated for the computation of similarity measures.

4.3.2. Stability and robustness against noise

In this section, the stability of the proposed algorithm is to be shown with respect to scale calculations. Furthermore, we present a noise test to prove the robustness against initial poses and noise.

The similarities between CFs of shapes are given in Fig. 14 when the reference shape is rescaled by using s ranging from 0.60 to 1.20. s_{op} calculated using the proposed technique is located in the peak area of the curves of the similarity measures. This suggests that minimizing the scale similarity measure in Eq. (12) based on the geometric moments of CFs, is numerically equivalent to maximizing the similarity measures with respect to s . However, as shown in Fig. 14 (left), there are fluctuations around the peak area of the curves. This is in fact caused by numerical errors. One reason is that for each manually chosen s , optimal values for \vec{q} and \vec{T} are recalculated. Another reason is that the rescaling of the reference shape is implemented by a simple nearest-neighbor interpolation algorithm. Boundary accuracy of shapes is therefore not ensured.

Fig. 15 shows the stability of the algorithm while the target shape is placed in a variety of poses. Every time the target '4' is in a new pose, the algorithm is used to register the reference '4' to the target. The group of quaternions that pose the target '4' is acquired by extracting the surface coordinates of a 4-D ball with the radius of 8 in a 4-D array (744 poses in total), and thus the poses are equally distributed in $SO(3)$. As demonstrated in Fig. 15, the reference '4' follows well while the target is in various poses.

However, little local fluctuations could be observed. These are mainly caused by the fact that while volumetric shape rotates, the number of voxels contained in the shape varies a little due to interpolation.

The result of the noise analysis is presented in Fig. 16. Using the same initial poses for shapes to be registered, the reference shape

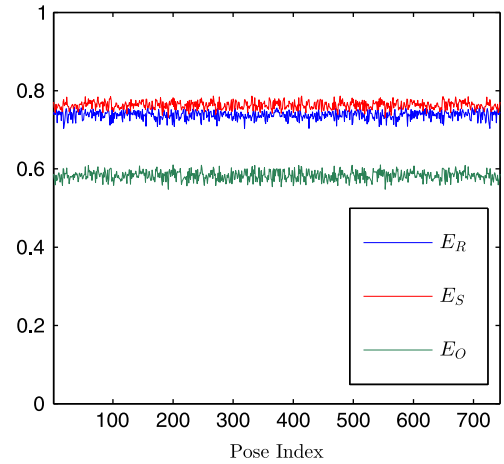


Fig. 15. Target shape with 744 poses (equally distributed in $SO(3)$) chosen to test the algorithm and the results presented by three similarity measures.

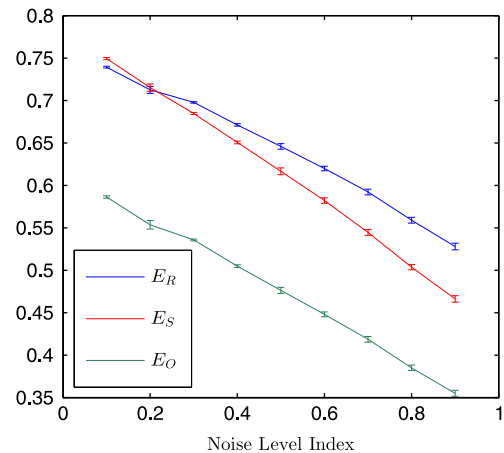


Fig. 16. The results of registration presented by the error plot of the three similarity measures while the target '4' is affected by increasing level of binary noise ('salt and pepper' noise).

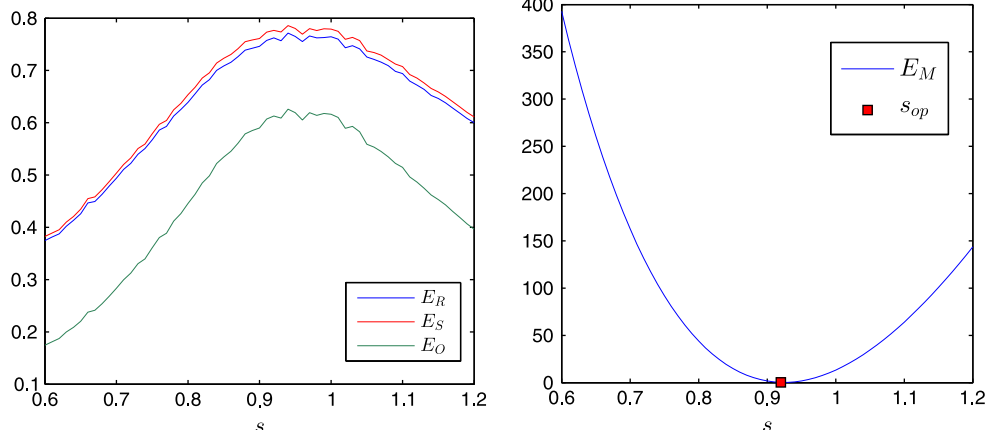


Fig. 14. Left: the inner product between shapes when s ranges from 0.60 to 1.20. s_{op} calculated when $M=5$ is 0.93. Right: s_{op} locates on the minimum of E_M , which indicates s_{op} that minimizes E_M also minimizes the inner product.

is to be registered to the target shape contaminated by binary noise ('salt and pepper' noise). The noise is generated inside the target shape 10 times at each level which ranges from 10% to 90%. For each level, the mean and variance of similarity measures are computed and these results are presented in Fig. 16. As observed from Fig. 16, the means of similarity measures decrease with the increasing level

of noise while the standard deviations remain very low, which indicates that our method is stable in the presence of excessive noise. Fig. 17 gives several examples of volumetric '4' with different levels of noise. It can be observed that high levels of noise (70% and 90%) cause severe topological defects of the target shape, while the method proposed here can still achieve accurate results.

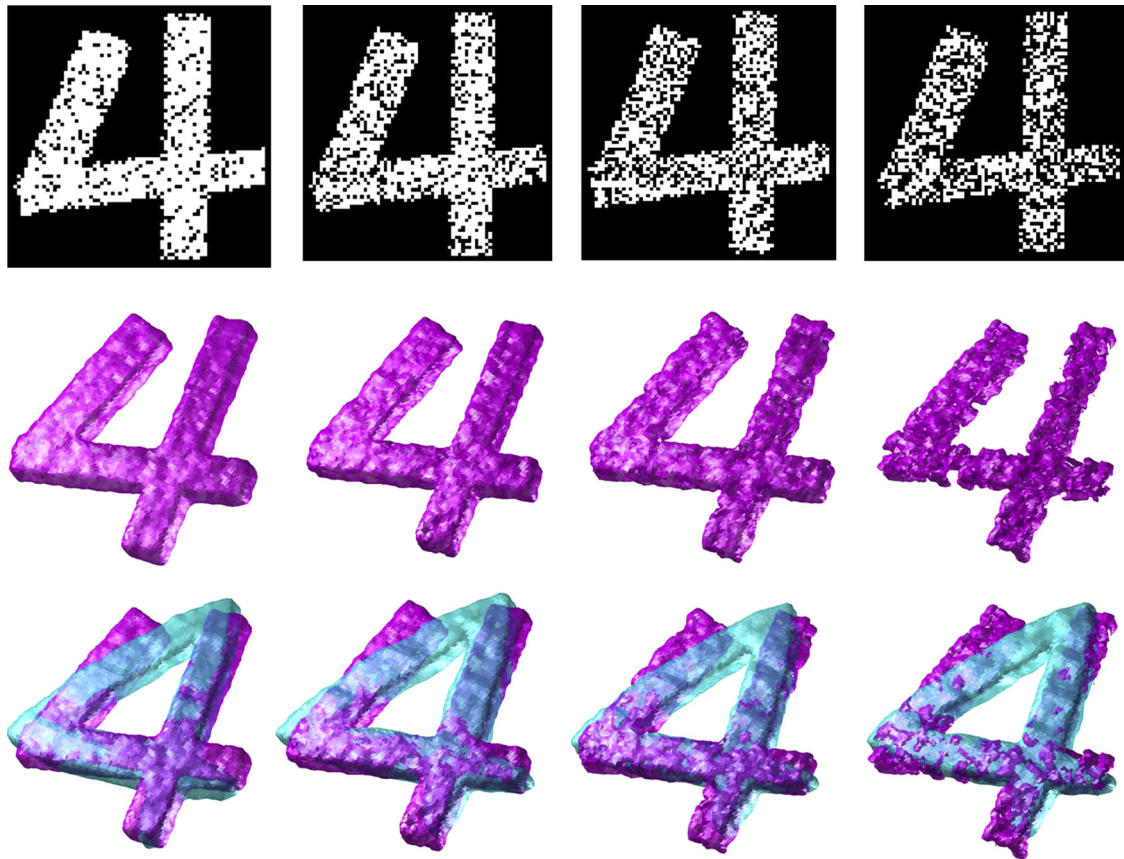


Fig. 17. Top row: the target '4' contaminated by 30%, 50%, 70%, and 90% level of noise from left to right (viewed from slice). Middle row: the target '4' with noises viewed in 3-D. Bottom row: the registration results corresponding to the noise levels.

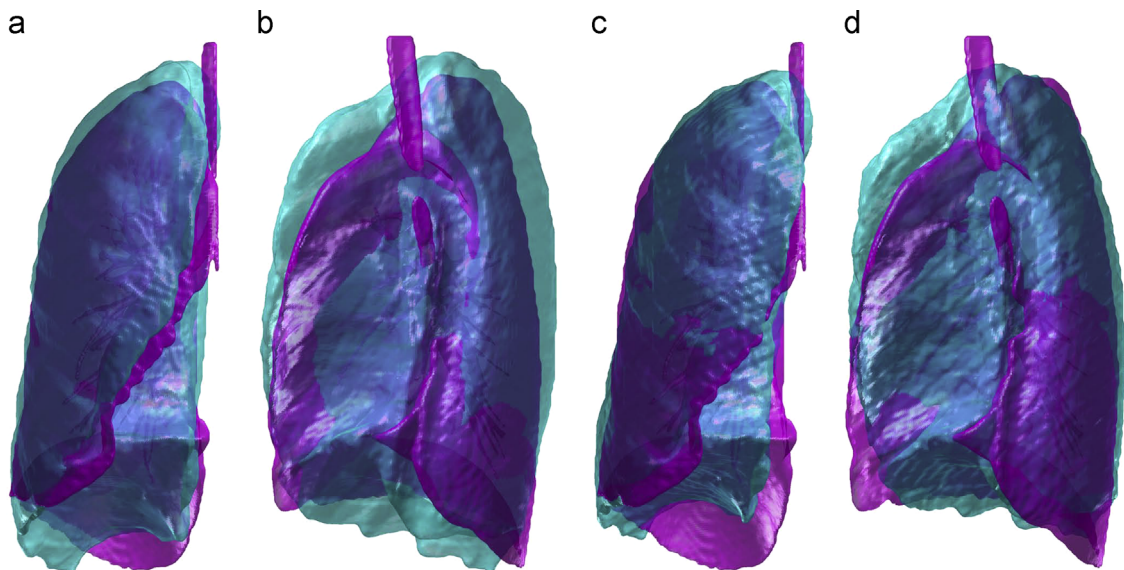


Fig. 18. (a) Overlapping of right lungs to be registered before registration. (b) Another view before registration. (c) Overlapping of right lungs after registration. (d) Another view after registration.

4.4. Examples of applications

4.4.1. Registration of reference and coarsely segmented lungs

Figs. 18 and 19 demonstrate the registrations of reference lungs and coarsely segmented lungs. The coarsely segmented lungs are obtained by thresholding HRCT (high resolution computed tomography) scans and finding the largest 18-connected region. The reference and the target lungs are from two patients. In respective registrations of the left and the right lungs, the other irrelevant half is masked out. As observed from Figs. 18 and 19, the method proposed here is barely affected by non-trivial noises (main airways outside and vessels inside).

4.4.2. Registration of a lung database

In this section, our method is applied to volumetric lungs in a lung database. The lung database consists of respectively 35 left and right lungs (70 lungs in total). This database covers a range of disease states, including spanning healthy, healthy smoker, mild COPD (chronic obstructive pulmonary disease) and moderate COPD.

Lungs in this database are manually segmented under expert supervision to ensure acceptable qualities and they are all represented by 3-D binary arrays (discrete CFs). Furthermore, due to the fact that the raw lung data are provided in various sizes, the process of adjusting all of the cases ready to be registered includes

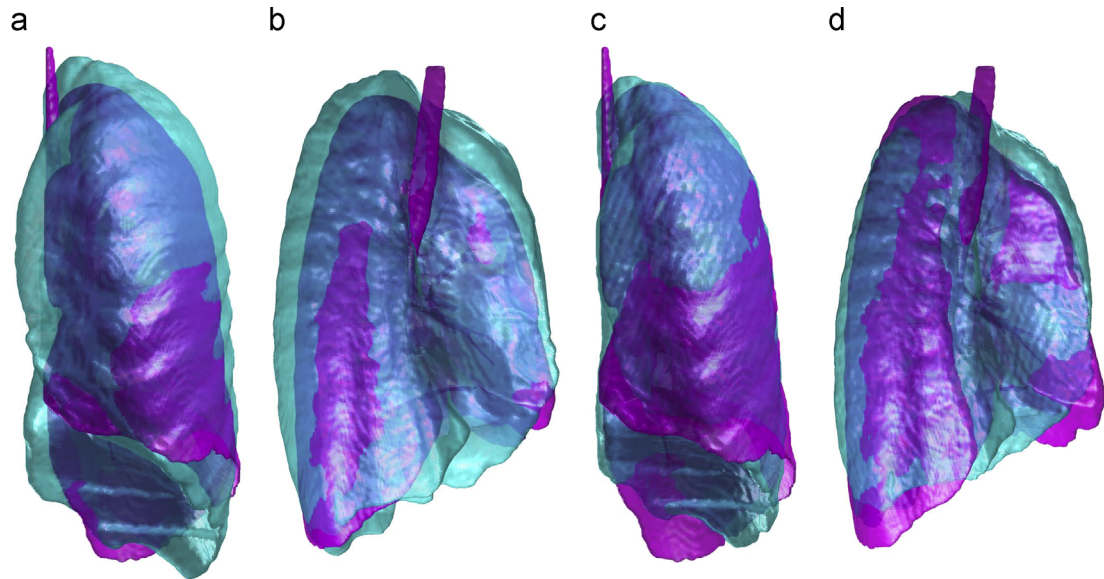


Fig. 19. (a) Overlapping of left lungs to be registered before registration. (b) Another view before registration. (c) Overlapping of left lungs after registration. (d) Another view after registration.

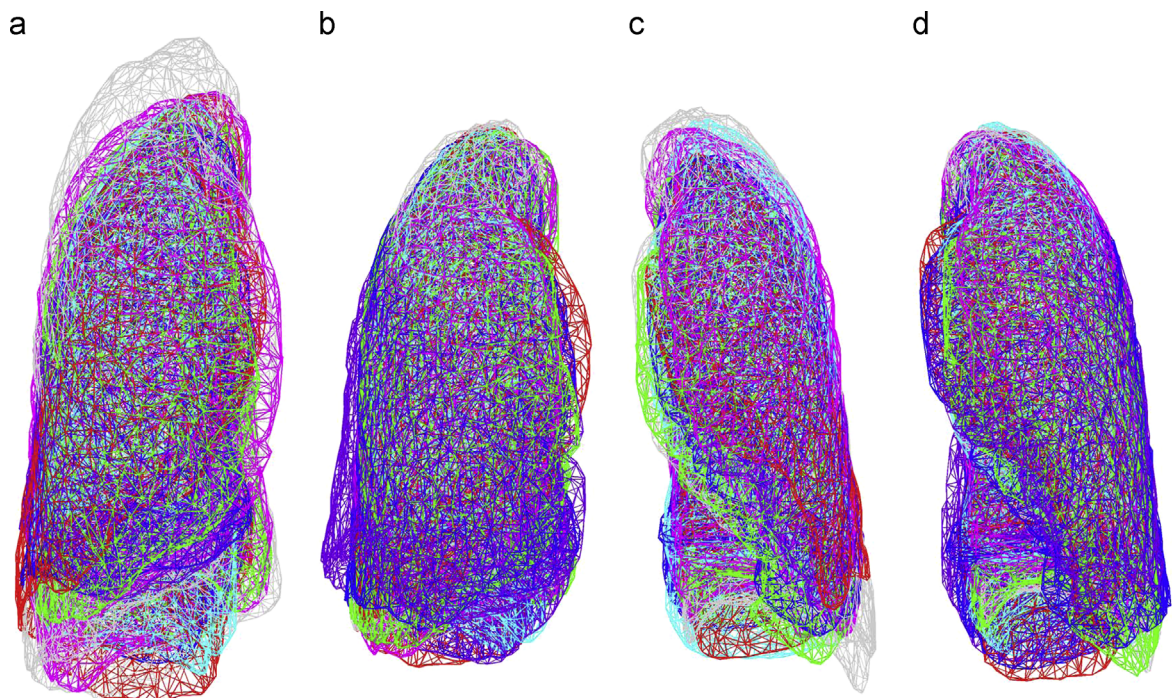


Fig. 20. (a) Several examples of overlapped right lungs before registration (center-of-mass alignment) using case 1 as the target shape. (b) Overlapped right lungs after registration. (c) Overlapped left lungs before registration (center-of-mass alignment). (d) Overlapped left lungs after registration.

extension of 3-D arrays and alignment of these lungs using their centers of mass.

The ‘leave-one-out’ scheme is employed here to perform the test: each lung is regarded as target while the other 34 lungs are reference shapes. There are 35 targets respectively for the group of right lungs and left lungs. The total number of registrations is therefore 2380. Several results of lung registration are visualized and presented in Fig. 20

Figs. 21–23 demonstrate a global view of the database registration. We here use ΔE_R , ΔE_O and ΔE_S , which are respectively the difference of E_R , E_O and E_S before and after registration using our method. It could be observed from these error plots that the

majority of the almost all values of means are above zero, while under certain conditions the algorithm did not deliver correct results. The percentage of successful cases of registration is

Table 2

The percentage of successful cases of registration with respect to each similarity measure for both left and right lungs.

	$\Delta E_R(\%)$	$\Delta E_O(\%)$	$\Delta E_S(\%)$
Left lungs	84.45	83.03	84.07
Right lungs	90.84	90.25	89.71

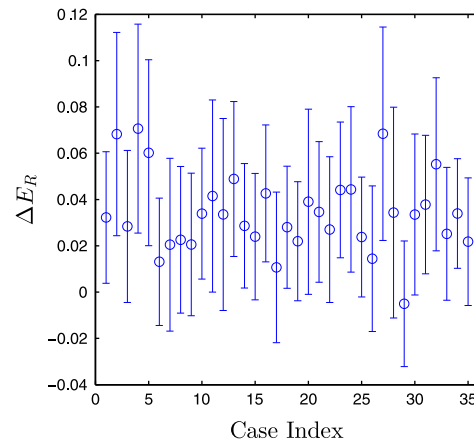
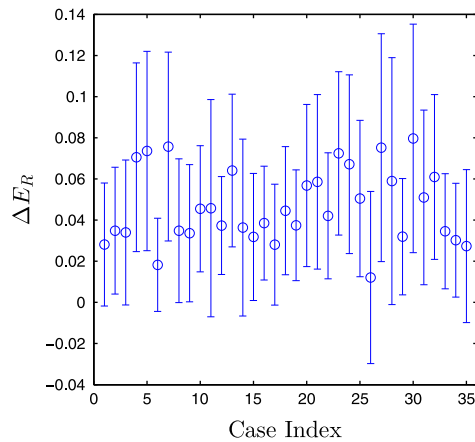


Fig. 21. Difference of E_R before and after registration for both left lungs (left) and right lungs (right).

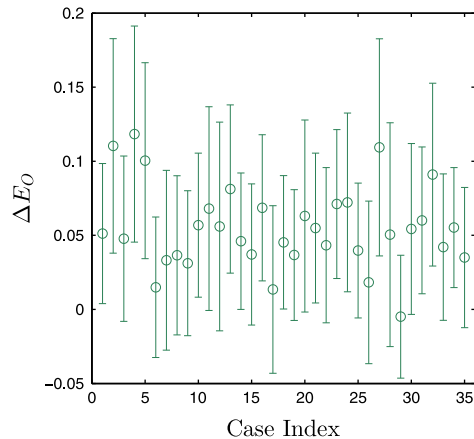
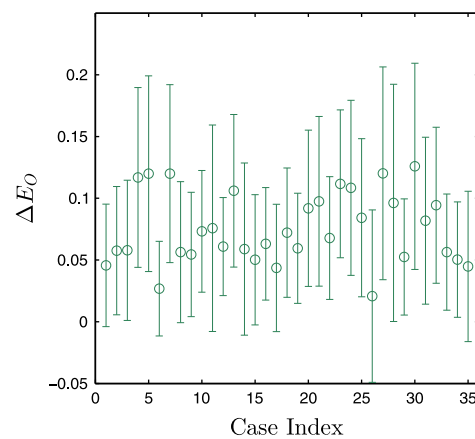


Fig. 22. Difference of E_O before and after registration for both left lungs (left) and right lungs (right).

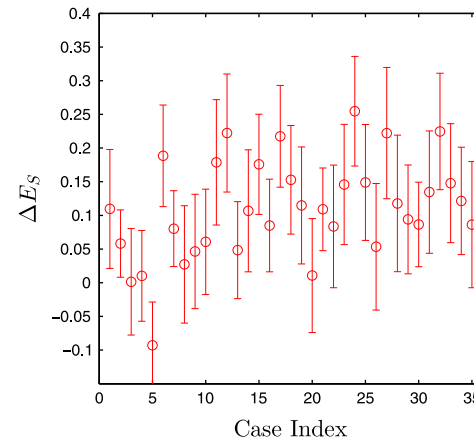
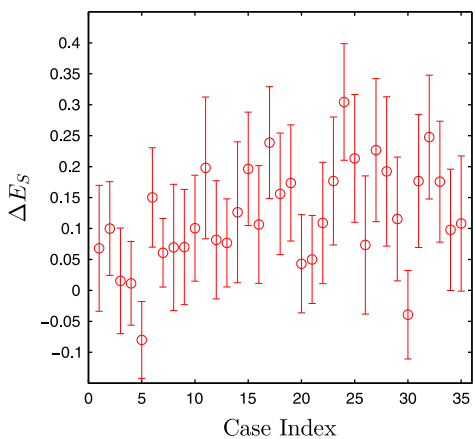


Fig. 23. Difference of E_S before and after registration for both left lungs (left) and right lungs (right).

presented in Table 2 with respect to each similarity measure for both left and right lungs. It should be noted that we strictly consider registrations with the difference of similarity measures before and after registration above 0 as successful cases, while failed cases have the differences very close to 0.

5. Conclusions and future works

This paper proposes a robust and fast registration technique of two volumetric shapes represented by CFs. PCA is employed to find principal axes associated with each shape. These principal axes provide a rotation and translation invariant transformation which largely facilitates the calculation of rotation parameters. Geometric moments are first employed to estimate scale parameter. Rotation and translation parameters are then calculated by maximizing the corresponding phase correlation terms, which take the advantage of FFT and make the method proposed here efficient.

We validate the method through three stages of the experiment: primary tests that concern registration of topologically different synthetic shapes, performance analyses that demonstrate accuracy, efficiency and stability of the method, and applications that show practical use of the method. Experimental results suggest that our method is able to register shapes with various topologies, robust to noise and initial poses, and efficient. However, a limitation of our work is that the ground truth of our lung database is not available. Nevertheless, successful registrations can be verified by examining ΔE_R , ΔE_O and ΔE_S over the entire database.

Regarding future directions, first, it is interesting to extend the method to perform non-rigid registration. Second, the method is to be incorporated into shape-based volumetric image segmentation which involves statistical modeling of training set and iterative registration during the segmentation process. This will allow us to have further understandings of the registration method proposed here.

Conflict of interest statement

None declared.

Acknowledgments

The HRCT data used in this work were acquired as a part of a study into the application of imaging to the characterization of the phenotypes of COPD. The written informed consent was given and signed by all subjects. The study was approved by the Southampton and South West Hampshire local research ethics committee (LREC number: 09/H0502/91) and the University Hospital Southampton Foundation Trust Research and development Department. The study was conducted in the Southampton NIHR Respiratory Biomedical Research Unit.

Appendix A

Lemma. The optimal rotation parameter \vec{q}_{op} calculated using Eq. (16) is scale invariant.

Proof. Since $s\mathbf{x} = sr\hat{\mathbf{x}}$, $\tilde{\chi}(s\mathbf{x})$ (rescaled version of $\tilde{\chi}(\mathbf{x})$) could be given in Ω_{s^2} as $\tilde{\chi}(sr, \hat{\mathbf{x}})$. Assuming that $\dot{r} = sr$, the s^2 map of

rescaled $\tilde{\chi}(\mathbf{r})$, denoted by $\tilde{\chi}_s(\hat{\mathbf{x}})$, satisfies:

$$\begin{aligned} \tilde{\chi}_s(\hat{\mathbf{x}}) &= \int_0^R \tilde{\chi}(sr, \hat{\mathbf{x}})r^2 dr \\ &= \int_0^R \tilde{\chi}(\dot{r}, \hat{\mathbf{x}}) \frac{\dot{r}^2}{s^2} d\frac{\dot{r}}{s} \\ &= \frac{1}{s^3} \int_0^R \tilde{\chi}(\dot{r}, \hat{\mathbf{x}})\dot{r}^2 d\dot{r} \\ &= \frac{1}{s^3} \tilde{\chi}(\hat{\mathbf{x}}) \end{aligned} \tag{A.1}$$

Let $\tilde{\chi}_{r_s}$ and $\tilde{\chi}_{t_s}$ be rescaled versions of $\tilde{\chi}_r$ and $\tilde{\chi}_t$ respectively using s_r and s_t , therefore, the equation below holds:

$$\langle \tilde{\chi}_{t_s}(\hat{\mathbf{x}}), \tilde{\chi}_{r_s}(\mathbf{R}(\vec{q})\hat{\mathbf{x}}) \rangle = \frac{1}{(s_r s_t)^3} \langle \tilde{\chi}_t(\hat{\mathbf{x}}), \tilde{\chi}_r(\mathbf{R}(\vec{q})\hat{\mathbf{x}}) \rangle \tag{A.2}$$

According to the above equation, rescaling of CFs causes the correlation term in Eq. (16) to multiply a constant $(1/(s_r s_t)^3)$. Therefore, \vec{q}_{op} that maximizes $\langle \tilde{\chi}_t(\hat{\mathbf{x}}), \tilde{\chi}_r(\mathbf{R}(\vec{q})\hat{\mathbf{x}}) \rangle$ also maximizes $\langle \tilde{\chi}_{t_s}(\hat{\mathbf{x}}), \tilde{\chi}_{r_s}(\mathbf{R}(\vec{q})\hat{\mathbf{x}}) \rangle$. \vec{q}_{op} calculated using Eq. (16) is thus scale invariant. □

Appendix B. Supplementary data

Supplementary data associated with this article can be found in the online version at <http://dx.doi.org/10.1016/j.patcog.2013.08.013>.

References

- [1] M. Al-Huseiny, S. Mahmoodi, M. Nixon, Robust rigid shape registration method using a level set formulation, *International Symposium in Visual Computing* (2010) 252–261.
- [2] P.J. Besl, N.D. McKay, A method for registration of 3-D shapes, *IEEE Transactions on Pattern Analysis and Machine Intelligence* 14 (2) (1992) 239–256.
- [3] D. Breitenreicher, C. Schnörr, Robust 3D object registration without explicit correspondence using geometric integration, *Machine Vision and Applications* 21 (5) (2010) 601–611.
- [4] X. Bresson, P. Vandergheynst, J.P. Thiran, A variational model for object segmentation using boundary information and shape prior driven by the Mumford–Shah functional, *International Journal of Computer Vision* 68 (2) (2006) 145–162.
- [5] T. Chen, B.C. Vemuri, A. Rangarajan, S.J. Eisenschenk, Group-wise point-set registration using a novel CDF-based Havrda-charvát divergence, *International Journal of Computer Vision* 86 (1) (2010) 111–124.
- [6] Y. Chen, H.D. Tagare, S. Thiruvankadam, F. Huang, D. Wilson, K.S. Gopinath, R. W. Briggs, E.A. Geiser, Using prior shapes in geometric active contours in a variational framework, *International Journal of Computer Vision* 50 (3) (2002) 315–328.
- [7] J. Diebel, Representing Attitude: Euler Angles, Unit Quaternions, and Rotation Vectors. Technical Report, Stanford University, Palo Alto, CA, 2006.
- [8] N. Gelfand, N.J. Mitra, L.J. Guibas, H. Pottmann, Robust global registration, in: *Proceedings of the Third Eurographics Symposium on Geometry Processing*, Eurographics Association, 2005, p. 197.
- [9] S. Granger, X. Pennec, Multi-scale EM-ICP: a fast and robust approach for surface registration, *Computer Vision–ECCV 2002* (2006) 69–73.
- [10] B. Gutman, Y. Wang, T. Chan, P.M. Thompson, A.W. Toga, et al., Shape registration with spherical cross correlation, in: *2nd MICCAI Workshop on Mathematical Foundations of Computational Anatomy*, 2008, pp. 56–67.
- [11] X. Huang, N. Paragios, D.N. Metaxas, Shape registration in implicit spaces using information theory and free form deformations, *IEEE Transactions on Pattern Analysis and Machine Intelligence* 28 (8) (2006) 1303–1318.
- [12] P.J. Kostelec, D.N. Rockmore, Fits on the rotation group, in: *Proceedings of Santa Fe Institute Working Papers Series Paper 03–11*, vol. 60, 2003.
- [13] W. Li, Z. Yin, Y. Huang, Y. Xiong, Automatic registration for 3D shapes using hybrid dimensionality-reduction shape descriptions, *Pattern Recognition* 44 (12) (2011) 2926–2943.
- [14] L. Lucchese, G. Doretto, G.M. Cortelazzo, A frequency domain technique for range data registration, *IEEE Transactions on Pattern Analysis and Machine Intelligence* 24 (11) (2002) 1468–1484.
- [15] Sasan Mahmoodi, Muayed S. Al-Huseiny, Mark S. Nixon, Similarity registration for shapes based on signed distance functions, in: *Advances in Visual Computing*, Springer, 2012, pp. 599–609.
- [16] S. Osher, J.A. Sethian, Fronts propagating with curvature-dependent speed: algorithms based on Hamilton–Jacobi formulations, *Journal of Computational Physics* 79 (1) (1988) 12–49.
- [17] N. Paragios, M. Rousson, V. Ramesh, Non-rigid registration using distance functions, *Computer Vision and Image Understanding* 89 (2–3) (2003) 142–165.

- [18] Martin Reuter, Hierarchical shape segmentation and registration via topological features of Laplace–Beltrami eigenfunctions, *International Journal of Computer Vision* 89 (2–3) (2010) 287–308.
- [19] Martin Reuter, Franz-Erich Wolter, Niklas Peinecke, Laplace–Beltrami spectra as shape-DNA of surfaces and solids, *Computer-Aided Design* 38 (4) (2006) 342–366.
- [20] Martin Reuter, Silvia Biasotti, Daniela Giorgi, Giuseppe Patanè, Michela Spagnuolo, Discrete Laplace–Beltrami operators for shape analysis and segmentation, *Computers & Graphics* 33 (3) (2009) 381–390.
- [21] S. Rusinkiewicz, M. Levoy, Efficient variants of the ICP algorithm, in: *Proceedings of 3-D Digital Imaging and Modeling Third International Conference*, 2001, pp. 145–152.
- [22] Raif M. Rustamov, Laplace–Beltrami eigenfunctions for deformation invariant shape representation, in: *Proceedings of the Fifth Eurographics Symposium on Geometry Processing*, Eurographics Association, 2007, pp. 225–233.
- [23] A. Segal, Dirk Haehnel, Sebastian Thrun, Generalized-ICP, in: *Proceedings of Robotics: Science and Systems (RSS)*, vol. 25, 2009, pp. 26–27.
- [24] José Silvestre Silva, Jaime B. Santos, Diogo Roxo, Paula Martins, Eduardo Castela, Rui Martins, Algorithm versus physicians variability evaluation in the cardiac chambers extraction, *IEEE Transactions on Information Technology in Biomedicine* 16 (5) (2012) 835–841.
- [25] M. Spiegel, D.A. Hahn, V. Daum, J. Wasza, J. Hornegger, Segmentation of kidneys using a new active shape model generation technique based on non-rigid image registration, *Computerized Medical Imaging and Graphics* 33 (1) (2009) 29–39.
- [26] Shanhui Sun, Christian Bauer, Reinhard Beichel, Automated 3-D segmentation of lungs with lung cancer in ct data using a novel robust active shape model approach, *IEEE Transactions on Medical Imaging* 31 (2) (2012) 449–460.
- [27] A. Tsai, A. Yezzi Jr., W. Wells, C. Tempany, D. Tucker, A. Fan, W.E. Grimson, A. Willsky, A shape-based approach to the segmentation of medical imagery using level sets, *IEEE Transactions on Medical Imaging* 22 (2) (2003) 137–154.
- [28] Y. Tsin, T. Kanade, A correlation-based approach to robust point set registration, *Computer Vision–ECCV*, 2004, pp. 558–569.
- [29] Y. Wang, K. Woods, M. McClain, Information-theoretic matching of two point sets, *IEEE Transactions on Image Processing* 11 (8) (2002) 868–872.

Wan-mu Liu received his B.Eng. in Biomedical Engineering from Jilin University, China, in 2010. In the same year, he joined in the Communications, Signal Processing and Control (CSPC) group in the School of Electronics and Computer Science (ECS) in University of Southampton, UK, pursuing a Ph.D. degree. His research interests are image segmentation, medical image processing and segmentation, volumetric registration and statistical modeling of shapes.

Sasan Mahmoodi received the B.Sc. degree from Amirkabir University of Technology in 1988, the M.Sc. degree from Sharif University of Technology, Tehran, Iran, in 1991, and the Ph.D. degree from the University of Newcastle, Newcastle upon Tyne, UK, in 1998. In 1999, he held a Research Fellowship post in mathematical analysis of human vision in the University of Newcastle upon Tyne. He joined the University of Southampton in 2007 as a Lecturer. His current research interests are in image processing, computer vision, Biometrics and modeling of the biological vision. Dr. Mahmoodi is a member of IEEE and the executive committee of BMVA.

Tom Havelock received a BMedSci (1996) and BMBS (1998) from Nottingham University. He became a member of the Royal College of Physicians in 2001 and was awarded the Diploma of Tropical Medicine and Hygiene from the University of London in 2002. He is currently taking time out from specialist clinical training in Respiratory Medicine to study for a Ph.D. at University of Southampton. At present he is working on methods to investigate the biological correlations of the topographical structural and functional variations that are identified in COPD using imaging. His research interests covering a number of fields based around patients with Chronic Obstructive Pulmonary Disease (COPD).

Michael J. Bennett was awarded a Ph.D. degree from the University of Edinburgh in signal processing techniques for real-time B-mode ultrasound imaging in cardiology in 2005. In 2004, he began his research career as a Research Associate at the University of Edinburgh. In 2005 he became a Research Fellow at the University of Edinburgh as a part of the Biologically Inspired Acoustic Systems (BIAS) project. Since 2009, Dr. Bennett has been a senior research scientist in the respiratory Biomedical Research Unit (BRU) at Southampton General Hospital. He is particularly involved in the development of techniques to support multi-modality image fusion to give the clinician additional information about the state of disease of the lung.